

# CONSIDERATION OF STRUCTURAL CONSTRAINTS IN PASSIVE ROTOR BLADE DESIGN FOR IMPROVED PERFORMANCE

Joon W. Lim

US Army Aviation Development Directorate - AFDD  
Aviation & Missile Research, Development & Engineering Center  
Research, Development and Engineering Command (RDECOM)  
Ames Research Center, Moffett Field, California, USA

## ABSTRACT

This study applied parameterization to rotor blade designs for improved performance. In the design, parametric equations were used to represent blade planform changes over the existing rotor blade model. Design variables included blade twist, sweep, dihedral, and the radial control point. Updates to the blade structural properties with changes in the design variables allowed accurate evaluation of performance objectives and realistic structural constraints - blade stability, steady moments (flap bending, chord bending, and torsion), and the high g maneuver pitch link loads. Performance improvement was demonstrated with multiple parametric designs. Using a parametric design with the advanced airfoils, the predicted power reduction was 1.0% in hover, 10.0% at  $\mu=0.30$ , and 17.0% at  $\mu=0.40$  relative to the baseline UH-60A rotor, but these were obtained with a 35% increase in the steady chord bending moment at  $\mu=0.30$  and a 20% increase in the half peak-to-peak pitch link load during the UH-60A UTTAS maneuver. Low vibration was maintained for this design. More rigorous design efforts, such as chord tapering and/or structural redesign of the blade cross section, would enlarge the feasible design space and likely provide significant performance improvement.

## INTRODUCTION

Rotorcraft, with their capability to take off and land practically anywhere, have demonstrated great versatility for civilian as well as military applications. Rotorcraft encounter unique challenges compared to fixed-wing aircraft due to widely varying flight conditions at which the main rotor is operated throughout the flight envelope. Improved design of the rotor blade is a key to overcome these challenges, but is difficult due to the complex nature of the aerodynamic and structural environments in the rotorcraft operational envelope.

There have been numerous optimization studies for rotor blades over the last three decades [1-12]. The common goals of these rotor optimization studies were a reduction of vibration and/or noise, a performance improvement, or a combination of these objectives. Recent applications of high fidelity CFD tools to rotorcraft have demonstrated a significant improvement in accuracy of the predictions [13]. With improved accuracy, a number of CFD-based optimization studies have been presented [6-12]. However, the design spaces in most of these optimization studies were limited since function evaluations in CFD tools were expensive. To overcome the limitation, an adjoint method [10, 11] was often adopted, which computes the gradient information at a small computation cost when gradient-based constrained optimization techniques were used.

Another commonly used approach to lower the computation cost is to reduce the number of design

variables by using a set of parametric equations [6-9]. These parametric equations are applied at multiple radial control points to morph the complex geometries in the passive blade design. The use of more radial control points makes the geometries of the parameterized passive rotor blade more accurate, although it substantially increases the computation time.

Imiela and Wilke [6] showed that the hover figure of merit of the EC1/EC2 rotor (5.5m in radius) was improved by 3.7% using variations of linear twist and anhedral at two radial locations,  $r/R=0.90$  and tip. The results were obtained using HOST/FLOWer and the optimizer DAKOTA [14]. The power required for the same rotor was reduced by 2.2% at 241 km/h ( $\mu=0.33$ ) using variations of twist, chord, sweep, and anhedral at the two fixed radial control points,  $r/R=0.90$  and tip (twist varied also at  $r/R=0.50$ ). In this study, structural property updates or use of constraints was not considered, so a risk of rotor blade structural failure existed.

Min et al. [8] presented a parametric study for noise reduction by applying a forward-backward sweep to the HART II rotor blade. Two parameters (forward sweep radial location and a forward sweep offset) were used to represent a design change, and up to about 40° sweep was considered. The results were obtained using GENCAS. The maximum BVI noise reduction of about 1 dB was found with the best design for the descent condition ( $\mu=0.15$ ). However, again, neither structural property updates nor use of constraints was considered.

Leon et al. [9] presented a more rigorous optimization study with sixteen design variables – twist, sweep, and chord at the five fixed radial control points plus the collective pitch. Parameterization was applied to the baseline ERATO blade configuration, and the results were obtained using HOST/elsA and DAKOTA. The hover figure of merit was improved by 0.06 after imposing a maximum steady pitch link load limit. However, they concluded that the optimum solution found from this aerodynamic design was an unrealistic s-shaped blade, which could have been avoided by considering additional structural and flight mechanics constraints.

Ortun et al. [12] made an attempt to include updates in the structural properties when design variables change. Parameterization was applied to the 7AD blade using a chord variation from  $r/R=0.30$  to tip with 10 Bezier poles. The optimum design after the update to the blade structural properties was presented with a forward sweep, but no structural constraints were considered. The results were computed using HOST and DAKOTA. The optimum solution indicated that a 3.3% power reduction was found at 140 knots ( $\mu=0.36$ ). Although a reasonable power reduction was shown, the optimized blade planform was still unrealistic. That was because no structural design constraints were included in the analysis.

The impact of blade structures with design changes has been frequently neglected in most rotorcraft optimization studies. With change in typical design variables (e.g., sweep or dihedral), the blade section structural properties change and consequently constraints such as blade stability boundaries and fatigue criteria need to be re-evaluated.

Passive rotor blade design changes blade geometries using design variables in order to meet the objective goals. Inclusion of realistic structural design constraints makes the feasible design space practical. The realistic structural constraints considered in this study are:

- Blade stability – blade damping in all modes should be positive.
- Steady (sectional) moments – these include the steady flap bending, lag bending, and torsion moments. The maximum design limits of these steady moments are typically unknown, so the constraints are bounded by the soft margin of being not excessively violated (e.g., 35%). This assumes that excessive design will be improved by future re-design of the blade structure via the cross sectional analysis.
- UTTAS (Utility Tactical Transport Aircraft System) maneuver half peak-to-peak pitch link

loads – The UTTAS maneuver is a high g maneuver condition for UH-60A flight. Similar to the steady moments, the constraint is bounded by the soft margin of being not excessively violated (e.g., 20%)

Although a formal optimization technique is not employed in this study, searching for an ad hoc optimal rotor design is attempted using a parametric study for the selected UH-60A flight condition. Significant validation efforts for the baseline UH-60A rotor are made using CAMARD II [15] to increase the confidence level on findings in this study. The primary objectives of this study are 1) to test the parametric design tool for application to passive rotor design, 2) to understand the effect of design variables on the structural constraints in passive rotor design, and 3) to find whether there exists a feasible design space within the structural constraints. These objectives will help establish guidelines for future applications of the optimization methodology to rotorcraft.

## PARAMETRIC DESIGN

Parametric design is applied to morph the complex geometries in the design with the use of a reduced number of design variables by means of a set of parametric equations. The advanced blade geometries such as British Experimental Rotor Programme (BERP) [16] or BlueEdge™ [17] can be modeled using parametric equations with many radial control points or higher order polynomials.

When sweep or dihedral is chosen as a design variable, the blade section will be rotated. If a rigid rotation is made in the blade section, the blade radius will be shortened and the section chord along the free stream direction will increase. Since the thickness of the airfoil section is kept the same, this approach would result in a different airfoil section. Therefore, the following design guidelines are used in the parametric design process to prevent any undesired outcomes:

- Blade hover tip Mach number is unchanged. Thus, the blade radius and rotor RPM need to be fixed.
- Blade airfoil section remains unchanged along the free stream direction.
- Blade solidity (geometric) is unchanged. Blade properties are scaled for constant solidity.

Parametric design is intended to make a change in blade planform with the use of a reduced number of design variables. For this process, parametric equations are established to characterize complex geometries of a rotor blade planform. Figure 1(a) shows a schematic diagram of a parametric blade with design variable  $D_j$  at the radial control point  $r_j$ . The design variables

considered are blade twist, chord taper, sweep, and dihedral with associated radial control point. In order to represent an unconventional blade planform or advanced blade tip geometry, up to four radial control points can be chosen in the present parametric design tool at which the design variables are varied. Thus, up to 20 design variables (4 variables at the 4 radial control points + the locations of all 4 radial control points) are allowed for parametric design. Complex examples of the parametric design are shown in Figs. 1(b)-(c). In these examples, parameterization was applied to the UH-60 wide chord blade configuration [18] with dual sweeps (forward-backward and backward-forward) as well as dihedral.

When parameterization is applied at the radial control point ( $r_j$ ), the blade section outboard of  $r_j$  is displaced or rotated. Figure 2 shows an example of the parametric design with the design variable  $D_j$  (i.e., sweep), describing how the basis of parametric equations is established. When design change is made at  $r_j$ , the old blade section coordinate ( $\eta_0, \zeta_0$ ) before design is rotated at  $r_j$  to the new coordinate ( $\eta_1, \zeta_1$ ). The airfoil section remains the same in the free stream direction after design. However, the structural cross section will have a narrower chord relative to the structural reference frame (e.g., elastic axis) but with the same section thickness. The designed beam section also becomes longer in order to maintain the same blade radius, but the solidity or structural mass remains the same.

The blade structural properties are updated using parametric equations. A transformation matrix,  $\mathbf{T}$ , in the parametric equation represents a kinematic relationship between the 'before' and 'after' designs, and is defined for each design variable:

$$\begin{Bmatrix} \eta_1 \\ \zeta_1 \end{Bmatrix} = \mathbf{T} \begin{Bmatrix} \eta_0 \\ \zeta_0 \end{Bmatrix} \quad (1)$$

where the subscript '0' and '1' imply before and after parametric design, respectively.

The next step is to update blade structural properties. Since these properties can be defined in any reference frame, we need a careful examination to identify the reference frame of the structural properties. Generally accepted definitions of structural properties are given in Ref. [19] with all structural properties referenced with the elastic axis.

Each of the blade structural properties ( $P_1$ ), after parametric design, is expressed in the following integral form for each design variable  $D_j$ :

$$P_1(D_j) = \iint_{A_1} f(\eta_1, \zeta_1, D_j) d\eta_1 d\zeta_1 \quad (2)$$

Update to the structural properties ( $P_1$ ) is made after substituting the parametric equation in Eq. (1) into Eq.

(2). Here, the new coordinate ( $\eta_1, \zeta_1$ ) is replaced with the old coordinate ( $\eta_0, \zeta_0$ ). As a result, new properties  $P_1$  will be explicitly given in terms of the known old properties and the design variable  $D_j$ . New properties  $P_1$  typically include the offsets, blade bending and torsion stiffness, and moment of inertias.

In a parametric study, the radial control point,  $r_j$  is typically fixed at  $r/R=0.40, 0.55, 0.70,$  or  $0.85$ , although it can vary when chosen as a design variable. Blade sweep is characterized by the quarter-chord line of blade, and is defined positive towards the trailing edge. Dihedral is defined positive blade tip up, and twist is positive leading edge (or nose) up. It is worth noting that a radial control point should be declared as the boundary of structural finite element and aerodynamic panel to avoid an irregularity of the properties inside the element or panel.

A notation for the parametric sequence of design variables uses the form,  $[D_1/D_2/D_3/D_4]_{V1234}$  where  $D_j$  ( $j = 1-4$ ) is the value of a design variable, the 'V' is the name of a design variable, and the '1, 2, 3, 4' indicates the location of active radial control point  $r_j$ . The 'V' indicates four different design variables - 'tw' for twist, 'sw' for sweep, 'dh' for dihedral, and 'tp' for taper ratio. The  $D_j$  will be removed in the parametric sequence if  $r_j$  is inactive. The parametric sequence is given as a sum if more than one design variable is applied. For example, the sequence is  $[-5]_{tw3} + [4]_{sw3}$  if  $-5^\circ$  twist and  $4^\circ$  sweep are applied at  $r_3$ .

## COMPREHENSIVE TOOL

CAMRAD II comprehensive analysis code [15] is used. The structural model is based on beam finite element formulation with each element having fifteen degrees of freedom. For the structural model, five nonlinear beam elements with one rigid element inboard the hinge are used. The section aerodynamic loads are based on lifting line theory with C81 table lookup and the ONERA EDLIN unsteady aerodynamic model. Yaw flow effect is also included. For the aerodynamic model, 23 aerodynamic panels are used with a free wake option. The trim solution is obtained at every  $15^\circ$  azimuth.

A propulsive trim is used for all calculations. As such, the trim targets are the specified thrust and propulsive force, and a zero roll moment. The trim variables are the collective, lateral and longitudinal cyclic pitch controls.

## VIBRATION INDEX

Vibratory hub forces and moments are transferred to the rotor pylon, and the vibration can be measured by means of the N per-rev components of the transferred hub forces and moments in the hub frame. The

intrusion index [20, 21] is a normalized frequency response based on the measured vibrations in the three orthogonal axes and represents the vibration at the three different locations in the aircraft under the four different flight conditions. The vibrations in the intrusion index are weighted differently for the three axes – 0.5 for the longitudinal and 0.67 for the lateral vibration relative to the vertical vibration. A generalized human factor vibration index is defined by adding the moment components to this intrusion index. The components are included up to 2N per–rev (2NP) for an N-bladed rotor (i.e., 8 per–rev for a 4-bladed rotor):

$$VI = \sum_{i=NP, 2NP} \left[ K_F \frac{F_{H,i}}{W_0} + K_M \frac{M_{H,i}}{RW_0} \right]$$

$$\text{where } F_{H,i} = \sqrt{(0.5F_{xH,i})^2 + (0.67F_{yH,i})^2} + F_{zH,i} \quad (3)$$

$$M_{H,i} = \sqrt{M_{xH,i}^2 + M_{yH,i}^2}$$

$F_H$  and  $M_H$  are the non-rotating hub forces and moments,  $W_0$  is the nominal aircraft weight, and  $R$  is the blade radius. In this study,  $K_F$  and  $K_M$  are set to unity.

## RESULTS AND DISCUSSION

The baselines used for parametric blade design are the UH-60A and UH-60 wide chord blade rotors. The design variables considered are blade twist, sweep, dihedral, and the location of the radial control point. A parametric study is performed by varying one of these design variables while the others are held fixed. The effects of design variables on performance objectives and structural constraints are examined. This section begins with validations of the baseline configuration to establish the level of confidence in accuracy when using a comprehensive analysis tool. To understand the effects of the design variables, three different parametric models are introduced. In-depth discussion will be made on the structural design constraints as well as performance objective functions.

The thrust, propulsive force, pitch link load, bending moments, and power are defined in non-dimensional forms as follows:

$$C_T = \frac{T}{\rho A (\Omega R)^2}, \quad C_x = \frac{X}{\rho A (\Omega R)^2}$$

$$C_{PL} = \frac{PL}{\rho A (\Omega R)^2}, \quad C_{Mk} = \frac{M_k}{\rho A (\Omega R)^2 R}$$

$$C_P = \frac{T}{\rho A (\Omega R)^3} \quad (4)$$

where  $A = \pi R^2$ , and

$$k = X(\text{torsion}), Y(\text{flap}), Z(\text{chord})$$

The thrust-weighted solidity used is 0.08471 for the UH-60A main rotor and 0.09248 for the UH-60 wide chord blade. A parametric study is performed by

simulating a moderately high-speed case for the UH-60A main rotor at an advance ratio of 0.30 (40x80 wind tunnel data, Run 52, Point 31) [22]. Power polar is computed over a full speed range from hover to high speed ( $\mu = 0.40$ ). A typical wind tunnel trim is used in earlier studies [23, 24], but in this study a propulsive trim is employed for performance analysis.

### Validation using UH-60A Main Rotor Data

A full-scale wind tunnel test of the UH-60A main rotor was completed in the USAF National Full-Scale Aerodynamics Complex (NFAC) 40- by 80-foot wind tunnel at NASA Ames Research Center [22]. The database from this test provides aerodynamic pressures, structural loads, control positions, rotor balance forces and moments, blade deformations, and rotor wake measurements. This extensive test data set is a useful resource for examination of the rotor behaviors in a wide range of flight conditions.

Figure 3 shows the UH-60A main rotor power polar correlated with the measured data (Run 52) covering advance ratios of 0.15 to 0.40. For performance calculation, a 3-DOF propulsive trim was used. To handle a different size of rotor, the trim targets in a non-dimensional form are scaled by (thrust-weighted) solidity. The performance prediction was made using CAMRAD II with a free wake model. The prediction seems well correlated with the measured data over a full speed range.

Figure 4 compares the  $M^2c_n$  and  $M^2c_m$  contours between the measured data and the prediction at  $\mu = 0.30$  (Run 52, Point 31). Compared to the measured data,  $M^2c_n$  prediction is higher near the  $0^\circ$  azimuth and also higher at the inboard of the blade in the 2<sup>nd</sup> quadrant. A phase shift of the negative down peak on the advancing side is seen from the  $M^2c_n$  prediction. The negative peak of  $M^2c_m$  on the advancing side is under-predicted. These discrepancies result from a deficiency of lifting line theory in the comprehensive code. It was demonstrated in Ref. [23] that the use of the CFD code (OVERFLOW 2) significantly improved the predictions.

Figure 5 shows the correlation of the non-dimensional oscillatory (the mean excluded) loads at  $r/R=0.30$  for an advance ratio of 0.30 (Run 52, Point 31). The loads include the flap bending, chord bending, torsion moment, and pitch link load. A positive sign convention used is blade tip bent up for flap bending moment, blade tip bent towards the trailing edge for chord bending moment, and blade tip twisted leading edge (or nose) up for torsion moment. Similar to Fig. 4, a phase shift of the down peak on the advancing side is observed for the flap bending and torsion moments as well as the pitch link load. For the chord bending moment, the prediction shows a large under-prediction.

Nonetheless, the peak-to-peak values are reasonably predicted by the comprehensive code. It was found in Ref. [24] that the prediction accuracy was significantly improved when using a CFD code although the discrepancy in chord bending moment was apparent even with a CFD code.

The UTTAS high g pull-up maneuver condition (C11029) in the UH-60A Airloads Flight Test program [25, 26] is used to investigate for the maximum design load of pitch link. The UTTAS maneuver begins near the maximum level flight speed, and achieves a normal load factor (2.1g) that significantly exceeds the steady-state lift limit of the rotor. After about 40 revolutions (9.4 seconds), the aircraft returns to the level flight (0.65g). The pitch link loads (oscillatory time history, mean, and half peak-to-peak) are compared with the measured data as shown in Fig. 6. Unexpectedly, a time delay by 3-4 rotor revolutions is observed in the prediction. The mean prediction showed a constant offset, and the half peak-to-peak of pitch link load displays under-prediction by 38%. The waveform of the half peak-to-peak matches the measured data when multiplied by a factor of 1.6. Although the discrepancy in the prediction is not small, the comprehensive results can be still used to estimate the maximum design loads in the UTTAS maneuver.

Some shortfalls in power and structural load correlations were found using the current analysis tool, CAMRAD II. However, power and structural load characteristics were reasonably estimated with these shortfalls. Thus, CAMRAD II is considered to be capable of carrying out this blade design study for improved performance.

### Parametric Design 1 (PD1)

To understand the effect of design variables, a parametric study was conducted by varying each design variable (twist, sweep, or dihedral) at the 3<sup>rd</sup> radial control point ( $r_j = 0.70R$ ) while the others were fixed over the baseline UH-60A rotor blade. Figure 7 shows a sketch of the UH-60A blade planform with two parametric blade designs – one with  $-4^\circ$  (forward) sweep and the other with  $8^\circ$  (backward) sweep. Since we applied a parametric design in an incremental form over the baseline configuration, the parametric blades maintain the original feature of the baseline.

Figure 8 compares total power of the UH-60A rotor with three design variables - twist, sweep, and dihedral. Main rotor total power and delta power relative to the UH-60A prediction are compared for the three parametric designs. The flight condition was at  $\mu = 0.30$  (Run 52 and Point 31). It is surprising to observe such a small sensitivity of power to twist. The prediction indicates that power is sensitive only to sweep. Applying a  $12^\circ$  sweep to the existing UH-60A

blade reduces power by 7.0%. A significant contribution to power reduction originates from the non-dimensional induced power ( $C_{pi}/s$ ). So, the parametric blade 1 (PD1) is defined as the UH-60A rotor with sweep variation, and its sensitivity to sweep will be explored.

Figure 9(a)-(b) shows time histories of  $M^2c_n$  and  $M^2c_m$  in the PD1 rotor at  $r/R=0.87$  when sweep is applied at  $r/R=0.70$  (Run 52, Point 31). As sweep increases, the sharp negative peak of  $M^2c_n$  on the advancing side shifts along the azimuth. Then, a new positive peak is formed near  $180^\circ$  azimuth. Similar harmonics are seen in  $M^2c_m$ . Figure 9(c)-(e) shows the 2-4/rev harmonics of  $M^2c_n$  along the blade span. As sweep increases, the 2/rev  $M^2c_n$  lowers at the inboard.

Contours of  $M^2c_n$ , non-dimensional induced power ( $C_{pi}/s$ ), and non-dimensional profile power ( $C_{po}/s$ ) are shown in Fig. 10. As sweep increases at  $r/R=0.70$ , the  $M^2c_n$  was re-distributed over the rotor disk: the negative peak of  $M^2c_n$  on the advancing side shifts toward the front of the rotor, the  $M^2c_n$  at  $0^\circ$  azimuth and in the 2nd quadrant gets significantly lower, and the  $M^2c_n$  in  $180^\circ$  azimuth becomes higher. These changes in  $M^2c_n$  are associated directly with the induced power. The profile power shows no meaningful change.

Next, torsion response is examined. Figure 11 shows time histories of the trimmed pitch control angle, the elastic twist at the blade tip and the total torsion response at the tip (Run 52, Point 31). As sweep increases, we expect that a negative (nose down) torsion moment is generated due to the aerodynamic lift in the swept part, and so is a negative torsion response. As expected, the trimmed pitch controls shows nose down responses on the advancing side as sweep increases. But, nose up responses are shown for the elastic twist, which is considered beneficial for forward flight performance. The total torsion is a sum of the pitch control and the elastic twist. Interestingly, the total torsion response shows a small variation with sweep changes to maintain a trim.

We observed a strong effect of sweep on power for the PD1 rotor. Now, the sensitivity of power to the location of sweep is explored. For this, the radial control point ( $r_j$ ) is varied from  $r/R=0.5$  to  $0.95$  with a sweep of  $8^\circ$ . The sensitivity of the PD1 rotor power is shown in Fig. 12 at  $\mu = 0.30$  (Run 52, Point 31). The rotor power reduces when the control point shifts inboard from the tip, but is almost unchanged inboard from  $r/R = 0.85$ .

Figure 13 compares time histories of the oscillatory flap bending (FBM), chord bending (CBM), and torsion (TM) moments at  $r/R=0.30$  in the PD1 rotor when sweep is applied at  $r/R=0.70$ . Time history of the

oscillatory pitch link load (PL) is also shown. The mean values were removed for oscillatory component calculations. The oscillatory flap bending moment is sensitive to sweep and the torsion moment is highly sensitive, whereas the oscillatory chord bending moment is barely sensitive. It is worth noting that the waveform of the pitch link load is almost identical to the torsion moment waveform at  $r/R=0.30$ .

A rotor designer needs to design a rotor blade to be operated within the maximum allowable design load. Exceeding the limit of the maximum design load, a rotor blade will undergo fracture or severe fatigue during operation. If a designer likes to increase the limit of the maximum design load, stiffening of the blade spar or other structural component reinforcement is required, which will result in an increase in the blade mass. Therefore, an examination of the limit of the maximum design load is important for new blade design.

Figure 14 shows the sectional steady flap bending, chord bending, and torsion moments as sweep increases. Sweep varies from  $-4$  to  $8$  degrees. The steady chord bending moment with the  $8^\circ$  sweep varied from  $r/R=0.95$  to  $0.70$  is also plotted along the blade span. The steady flap bending moment is found not sensitive. Introduction of sweep rapidly increases negative chord bending (chord lead) moment due to the off-axis centrifugal force in the swept part. The maximum steady chord bending moment at  $r/R = 0.70$  increases by a factor of 15 for  $4^\circ$  sweep and by 22 for  $8^\circ$  sweep. When the radial control point of the  $8^\circ$  sweep shifts outboard from  $r/R=0.70$ , the steady chord bending moment rapidly reduces. A sweep effect is complicated for torsion. As seen in Fig. 11, an increase in sweep generated a positive elastic twist and so a positive torsion moment. Thus, in the figure the positive torsion moment is observed inboard as sweep increases.

Figure 15 shows the vibrations contributed from the individual components of the 4 and 8 per-rev hub forces and the vibration index. For a 4-blade rotor, the 4/rev component contribution to the vibration index is expectedly higher than the 8/rev, and among the 4/rev components the 4/rev vertical shear contribution is highest. Note that the contribution from the 8/rev vertical shear is not negligible.

The blade frequencies and damping with design variables – twist, sweep, dihedral, and radial control points - are examined in Fig. 16. Strong frequency coalescences are observed among the 1<sup>st</sup> torsion, 2<sup>nd</sup> lag, and 3<sup>rd</sup> flap modes in all the cases due to the couplings in flap-torsion, extension-flap, and extension-lag. So, the dampings are strongly coupled between those modes. When sweep increases to 12 degrees, the damping of the 2<sup>nd</sup> and 4<sup>th</sup> flap modes

rapidly shift towards the instability region (see Fig. 16(b)). When the radial control point (with  $8^\circ$  sweep) shifts from the initial position at  $r/R=0.70$  to the outboard, the instability diminishes (see Fig. 16(d)).

The sensitivity of the power and constraints was examined for the PD1 rotor. This PD1 rotor was based on the UH-60A rotor. The sensitivity of a more rigorous rotor design will be examined using the PD2 rotor that is based on the UH-60 wide chord blade with advanced airfoils.

### Parametric Design 2 (PD2)

The UH-60 wide chord blade has an all-composite graphite/glass-tubular spar with an increased chord (10% increase in solidity), advanced airfoils (SC2110 and SSCA09), and a swept-tapered tip with anhedral [18, 27]. With an increased chord, the aircraft payloads were significantly increased.

Figure 17 shows the sensitivity of total power to three design variables - twist, sweep, and dihedral - for the wide chord blade rotor. For the sensitivity representation, the total power was divided by the maximum power at  $10^\circ$  twist. Parameterization was applied at one control point ( $r_j = 0.70R$ ) over the wide chord blade. Simulations were made for the 40x80 UH-60A condition at  $\mu = 0.30$  (Run 52 and Point 31). The power of the wide chord blade is sensitive to all the design variables, although little sensitivity to twist or dihedral was found with the UH-60A rotor (see Fig. 8).

Since a sensitivity of total power was found to all the design variables, all these design variables were included in the parametric design PD2 by introducing  $6^\circ$  twist and  $8^\circ$  dihedral at the (third) radial control point ( $r/R=0.70$ ) with sweep variation. Selection of the specific values of design variables was an ad hoc choice for demonstration purpose. A naming convention used is that 'PD2' is a family of the specific parametric design with sweep allowed varying, and 'FPD2' is a final PD2 design after the sweep is determined.

A sensitivity of power for the PD2 rotor is explored with a sweep variation ( $-4$  to  $8^\circ$ ) at  $r/R=0.70$  as shown in Fig. 18. As we found earlier, total power is sensitive to sweep and most of the power reduction originates from the induced power. A choice of sweep is limited not to generate too large steady chord moment. The final PD2 blade (FPD2) is decided with a sweep of  $2^\circ$  at  $r/R=0.70$  in the PD2 family. As seen in this figure, at the  $2^\circ$  sweep the performance is not at optimum (11% power reduction relative to the UH-60A prediction), but we expect the steady moments reduce. Figure 19 shows a sketch of the FPD2 blade along with the PD2 designs with  $-4^\circ$  and  $8^\circ$  sweep. For convenience, this

FPD2 blade is denoted as  $[6]_{tw3} + [2]_{sw3} + [8]_{dh3}$  where the subscript indicates the design variable and the radial control point number.

The sectional steady blade bending and torsion moments could potentially exceed the limit of the maximum design load after parametric design. Thus, a sensitivity of the steady structural loads is examined for the PD2 rotor. The PD2 steady blade moments along the blade span are shown in Fig. 20 with sweep variation (Run 52 and Point 31,  $\mu=0.30$ ). We observed earlier in Fig. 14 that sweep significantly increased the steady chord bending moment (CBM) and moderately increased the steady torsion moment (TM) inboard while little sensitivity was found for the steady flap bending moment (FBM). The same trend is found here. In fact, the steady chord bending moment increases from -0.00058 to -0.00138 (240% increase) for a 4° sweep and to -0.00249 (433% increase) for an 8° sweep. Note that the computed steady chord bending moment in the wide chord blade baseline configuration was -0.00058. On the other hand, the torsion moment shows a moderate sensitivity to sweep, which appears dominated by the aerodynamic sweep effect (the lift times the offset due to sweep).

The steady flap bending moment shows a sharp spike at  $r/R=0.70$ , although it is not sensitive to sweep (see Fig. 20). At first, this spike surprised us, so further investigation was made. The sharp spike was found due to a flap bending moment generated by a centrifugal force in the dihedral part of the blade (8° dihedral in the PD2 blade). Thus, the effect of dihedral on the steady flap bending moment is examined as shown in Fig. 21. The maximum magnitude of the steady flap bending moment increases by a factor of 2.4 for a 4° dihedral and 5.4 for an 8° dihedral.

Although a large reduction of power was made for the FPD2 rotor, the steady moment constraints were significantly violated. It appears that shifting the radial control point outboard from  $r/R=0.70$  will help to reduce the steady moments. The next blade design, PD3 will have the radial control point shifted outboard from the PD2 rotor.

### Parametric Design 3 (PD3)

The steady moments rapidly increase with an introduction of either sweep or dihedral due to centrifugal force. This increase in the steady moments significantly limits the feasible design space during rotor blade design. To reduce the steady moments, two key changes are made from the PD2 design - the dihedral is lowered from 8° to 4°, and the radial control point shifts from  $r/R=0.70$  to 0.85, while the twist increases from 6° to 10°. So, the resulting parametric design 3 (PD3) has a 10° twist and a 4° dihedral at the

fourth radial control point ( $r/R=0.85$ ) over the wide chord blade with sweep allowed varying.

Figure 22 compares total power of the PD2 and PD3 rotors with sweep variation for the UH-60A condition (Run 52 and Point 31,  $\mu=0.30$ ). Although the total power of both the PD2 and PD3 rotors slowly reduces as sweep increases, the PD3 power is generally higher than the PD2 power. This is because of a trade-off in design between power and steady moments. The final PD3 design (FPD3:  $[10]_{tw4}+[4]_{sw4}+[4]_{dh4}$ ) is chosen with 4° sweep. Figure 23 shows a sketch of the FPD3 rotor blade design.

Figure 24 compares power polar between the FPD2 and FPD3 rotors against the UH-60A main rotor power prediction. As observed in Figs. 20 and 21, the FPD2 rotor has shown significant increases in the steady moments from the baseline wide chord blade rotor configuration. Since the FPD3 rotor was designed to improve the steady moment issue found in the FPD2 rotor, its rotor power is expected higher than FPD2 as a trade-off. This happened as shown in the figure, but in hover and at  $\mu=0.40$  the FPD3 power is unexpectedly slightly lower than the FPD2. The FPD3 power reduction is 1.0% in hover, 10.0% at  $\mu=0.30$ , and 17.0% at  $\mu=0.40$ , relative to the UH-60A power. This power reduction is largely owing to the use of advanced airfoils. Thus, the power of the UH-60A rotor with the advanced airfoils was compared in Fig. 25. The benefit of the blade planform change alone can be roughly estimated by the difference of power between the UH-60A rotor having the advanced airfoils and the FPD3 rotor. Thus, the planform change in the FPD3 rotor could offer reductions of 0.5% in hover, 2.7% at  $\mu=0.30$ , and 4.9% at  $\mu=0.40$  against the UH-60A rotor.

Contours of  $M^2c_n$ , induced power ( $C_{pi}/s$ ), and profile power ( $C_{po}/s$ ) in the PD3 design are shown in Fig. 26 at  $\mu=0.30$  (Run 52, Point 31). Small sensitivity to sweep variation is found from  $M^2c_n$  and the induced power. The induced power at the 0° azimuth gets lower as sweep increases.

Figure 27 compares time histories of the oscillatory flap bending (FBM), chord bending (CBM), and torsion (TM) moments at  $r/R=0.30$  in the PD3 rotor with the sweep varied from -2° to 8°. The oscillatory pitch link load (PL) is also shown. The same UH-60A flight condition is used (Run 52 and Point 31,  $\mu=0.30$ ). The oscillatory torsion moment and so the pitch link load shows sensitivity with sweep variation, but their peak-to-peak values stay almost the same.

The steady chord bending moment (CBM) in the PD3 rotor is expected to decrease significantly with the location of the sweep control point shifted from  $r/R =$

0.70 to 0.85. In Fig. 28, adding a 4° (backward) sweep at  $r/R=0.85$  shows an increase in the maximum steady chord bending moment from -0.00052 to -0.00079 (in magnitude; 52% increase). This magnitude increase to -0.00079 is equivalent to a 35% increase relative to the wide chord blade baseline value (-0.00058). However, we do not have sufficient information for judgment whether this maximum bending load increase will cause a structure failure or not, so further investigation on this matter is necessary.

Figure 29 compares the vibration index between the UH-60A and PD3 design (Run 52, Point 31). The PD3 design maintains a low vibration level as sweep increases. A sharp rise in vibration is found from the UH-60A rotor when sweep is introduced.

Figure 30 shows the frequencies and damping ratios of the PD3 rotor with sweep variation. The frequencies appear coupled between the 2<sup>nd</sup> lag and 3<sup>rd</sup> flap modes and between the 1<sup>st</sup> torsion and 2<sup>nd</sup> flap modes. All the modes appear stable with sweep variation.

Figure 31 shows the mean and half peak-to-peak values of pitch link load for the UTTAS pull up condition (C11029) with sweep variation. The mean pitch link load is not sensitive to sweep, but the half peak-to-peak magnitude is sensitive. An introduction of a 4° sweep at  $r/R=0.85$  in the PD3 design (FPD3) increases the half peak-to-peak pitch link load from 0.010 to 0.012 (20% increase). This increase could be accepted if the blade stiffness is reinforced at the sections. From all these findings, we observed that an introduction of sweep or dihedral in the blade design would increase the sectional steady moments due to centrifugal force. To overcome this difficulty, more rigorous design efforts are necessary by re-distributing of the blade section mass by means of chord tapering or performing structural redesign of the blade cross sections.

## CONCLUSIONS

This study applied parameterization to rotor blade designs for improved performance. In the design, parametric equations were used to represent blade planform changes over the existing rotor blade model. Complex geometries of a rotor blade were successfully simulated using the present parametric design tool.

UH-60A and UH-60 wide chord blade rotors were used as the baseline configurations for parametric blade design. Design variables included blade twist, sweep, dihedral, and the radial control point. Updates to the blade structural properties with changes in the design variables allowed accurate evaluation of performance objectives and realistic structural constraints - blade stability, steady moments (flap

bending, chord bending, and torsion), and the UTTAS maneuver pitch link loads.

Performance improvement was demonstrated with multiple parametric designs. Adopting advanced airfoils for the UH-60A rotor resulted in a power reduction by 0.5% in hover, 7.3% at  $\mu=0.30$ , and 12.1% at  $\mu=0.40$ . Using the best design (FPD3) with the advanced airfoils in the present study, the predicted power reduction was 1.0% in hover, 10.0% at  $\mu=0.30$ , and 17.0% at  $\mu=0.40$  relative to the baseline UH-60A rotor. But these were obtained with a 35% increase in the steady chord bending moment at  $\mu=0.30$  and a 20% increase in the half peak-to-peak pitch link load during the UTTAS maneuver. Low vibration was maintained for the PD3 rotor.

The structural constraints often confined the design space and governed the optimal solutions. A key for a better solution is to find the feasible design space which is less dependent on these constraints. More rigorous design efforts, such as chord tapering and/or structural redesign of the blade cross section, would enlarge the feasible design space and likely provide significant performance improvement.

## ACKNOWLEDGMENTS

The author would like to express many special thanks to Wayne Johnson, NASA Ames Research Center and Thomas Maier, AFDD for their invaluable insights, guidance, and encouragement until completion of this work.

## REFERENCES

- <sup>1</sup>Lim, J. W., and Chopra, I., "Aeroelastic Optimization of a Helicopter Rotor Using an Efficient Sensitivity Analysis," *Journal of Aircraft*, Vol. 28, No. 1, January 1991, pp. 29-37.
- <sup>2</sup>Celi, R. and Friedmann, P. P., "Structural Optimization with Aeroelastic Constraints of Rotor Blades with Straight and Swept Tips," *AIAA Journal*, Vol. 28, No. 5, 1990, pp. 928-936.
- <sup>3</sup>Friedmann, P. P., "Helicopter Vibration Reduction Using Structural Optimization with Aeroelastic / Multidisciplinary Constraints - A Survey," *Journal of Aircraft*, Vol. 28, No. 1, January 1991, pp. 8-21.
- <sup>4</sup>Celi, R., Recent Applications of Design Optimization to Rotorcraft - A survey, *Journal of Aircraft*, Vol. 36, No. 1, January-February 1999, pp.176-189.
- <sup>5</sup>Ganguli, R., Survey of Recent Developments in Rotorcraft Design Optimization, *Journal of Aircraft*, Vol.41, No. 3, May-June 2004, pp. 493-510.
- <sup>6</sup>Imiela, M., and Wilke, G., "Passive Blade Optimization and Evaluation in Off-Design Conditions," 39<sup>th</sup> European Rotorcraft Forum Proceedings, Moscow, Russia, September 3-5, 2013.

- <sup>7</sup> Johnson, C. S., and Barakos, G. N., "Optimising Aspects of Rotor Blades in Forward Flight," Proceedings of the 49<sup>th</sup> AIAA Aerospace Sciences Meeting including the New Horizons Forum and Aerospace Exposition, January 4-7, 2011, Orlando, Florida.
- <sup>8</sup> Min, B. Y., Sankar, L. N., Collins, K., and Brentner, K. S., "CFD-CSD Coupled Study in the BVI Characteristics of a Saw-Tooth Blade Planform," American Helicopter Society 67<sup>th</sup> Annual Forum Proceedings, Virginia Beach, Virginia, May 3-5, 2011.
- <sup>9</sup> Leon, E.R., Le Pape, A., Desideri, J., Alfano, D., and Costes, M., "Concurrent Aerodynamic Optimization of Rotor Blades Using a Nash Game Method," American Helicopter Society 69<sup>th</sup> Annual Forum Proceedings, Phoenix, Arizona, May 21-23, 2013.
- <sup>10</sup> Mishra, A., Mani, Karthik, Mavriplis, D., and Sitaraman, J., "Time-dependent Adjoint-based Aerodynamic Shape Optimization Applied to Helicopter Rotors," American Helicopter Society 70<sup>th</sup> Annual Forum Proceedings, Montreal, Canada, May 20-22, 2014.
- <sup>11</sup> Naik, K.R., Economon, T.D., Colonno, M.R., Palacios, F., and Alonso, J.J., "A Time-Spectral Adjoint Formulation for Shape Optimization of Helicopters in Forward Flight," American Helicopter Society 69<sup>th</sup> Annual Forum Proceedings, Phoenix, Arizona, May 21-23, 2013.
- <sup>12</sup> Ortun, B., Bailly, J., des Rochettes, H.M., and Delrieux, Y., "Recent Advances in Rotor Aerodynamic Optimization, Including Structural Data Update," 5<sup>th</sup> Decennial American Helicopter Society Specialists' Conference Proceedings, San Francisco, California, January 22-24, 2014.
- <sup>13</sup> Potsdam, M., Yeo, H., and Johnson, W., "Rotor Airloads Prediction Using Loose Aerodynamic / Structural Coupling," *Journal of Aircraft*, Vol. 43, (3), May-June 2006, pp. 732-742.
- <sup>14</sup> Adams, B. "The dakota toolkit for parallel optimization and uncertainty analysis," SIAM Conference on Optimization Proceedings, Boston, MA, May 2008.
- <sup>15</sup> Johnson, W., "Rotorcraft Aerodynamic Models for a Comprehensive Analysis," Proceedings of the 54<sup>th</sup> Annual Forum of the American Helicopter Society, Washington, D.C., May 20-22, 1998.
- <sup>16</sup> Brocklehurst, A., and Barakos, G.N., "A Review of Helicopter Rotor Blade Tip Shapes," *Progress in Aerospace Sciences*, Elsevier Company, Vol. 56, 2013, pp. 35-74.
- <sup>17</sup> Rauch, P., Gervais, M., Cranga, P., Baud, A., Hirsch, J-F, Walter, A., and Beaumier, P., "Blue Edge™: The Design, Development, and Testing of a New Blade Concept," American Helicopter Society 67<sup>th</sup> Annual Forum Proceedings, Virginia Beach, Virginia, May 3-5, 2011.
- <sup>18</sup> Shinoda, P. M., Norman, T. R., Jacklin, S. A., Yeo, H., Bernhard, A. P. F., and Haber, A., "Investigation of a Full-Scale Wide Chord Blade Rotor System in the NASA Ames 40- by 80-Foot Wind Tunnel," American Helicopter Society 4<sup>th</sup> Decennial Specialist's Conference on Aeromechanics Proceedings, San Francisco, CA, January 21-23, 2004.
- <sup>19</sup> Hodges, D.H., and Dowell, E.H., "Nonlinear Equations of Motion for the elastic Bending and Torsion of Twisted Nonuniform Rotor Blades," NASA TN D-7818, December 1974.
- <sup>20</sup> Crews, S.T., and Hamilton, B.W., "Army Helicopter Crew Seat Vibration – Past Performance, Future Requirements," Proceedings of the American Helicopter Society North East Region National Specialists' Meeting on Helicopter Vibration, Hartford, Connecticut, Nov. 1981.
- <sup>21</sup> Anonymous, "Requirements for Rotorcraft Vibration, Specifications, Modeling and Testing," Aeronautical Design Standard ADS-27A-SP, US Army Aviation Systems Command, Redstone Arsenal, Alabama, May 2006.
- <sup>22</sup> Norman, T. R., Shinoda, P., Peterson, R. L. and Datta, A., "Full-Scale Wind Tunnel Test of the UH-60A Airloads Rotor," American Helicopter Society 67<sup>th</sup> Annual Forum Proceedings, Virginia Beach, Virginia, May 3-5, 2011.
- <sup>23</sup> Romander, E., Norman, T. R., and Chang, I-C., "Correlating CFD Simulation With Wind Tunnel Test for the Full-Scale UH-60A Airloads Rotor," American Helicopter Society 67<sup>th</sup> Annual Forum, Virginia Beach, VA, May 3-5, 2011.
- <sup>24</sup> Yeo, H., and Romander, E.A., "Loads Correlation of a Full-Scale UH-60A Airloads Rotor in a Wind Tunnel," American Helicopter Society 68<sup>th</sup> Annual Forum Proceedings, Fort Worth, Texas, May 1-3, 2012.
- <sup>25</sup> Bousman, W. G., and Kufeld, R. M., "UH-60A Airloads Catalog," NASA TM-2005-212827, August 2005.
- <sup>26</sup> Bhagwat, M.J., and Ormiston, R.A., "Examination of Rotor Aerodynamics in Steady and Maneuvering Flight Using CFD and Conventional Methods," American Helicopter Society Specialist's Conference on Aeromechanics Proceedings, San Francisco, CA, January 2008.
- <sup>27</sup> Yeo, H., Bousman, W.G., and Johnson, W., "Performance Analysis of a Utility Helicopter with Standard and Advanced Rotors," American Helicopter Society Aerodynamics, Acoustics, and Test an Evaluation Technical Specialists Meeting Proceedings, San Francisco, CA, January 2002.

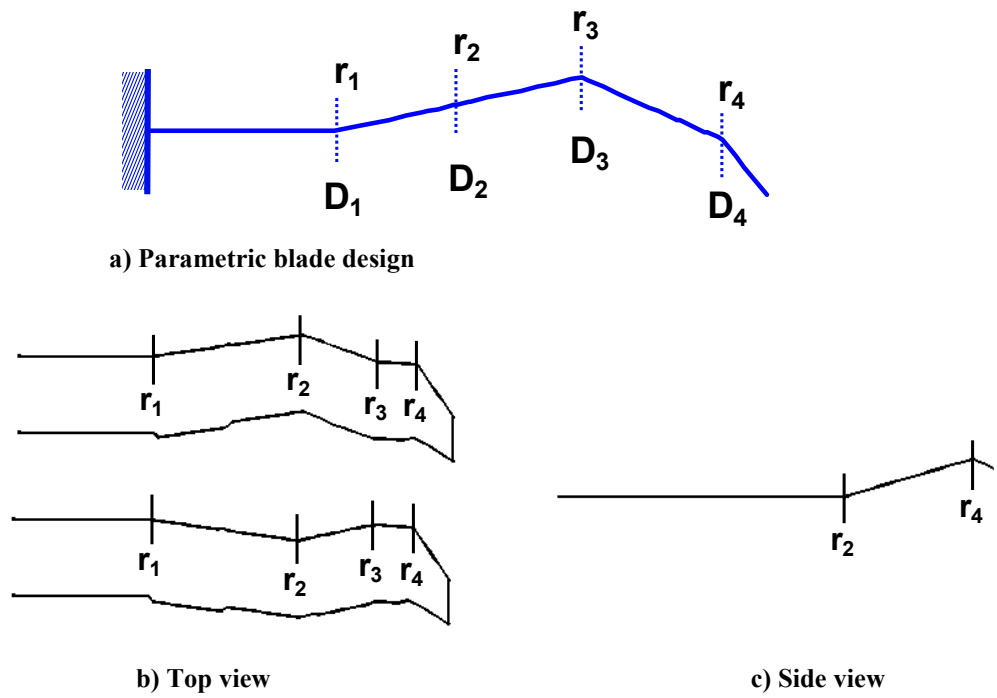


Figure 1. Examples of parametric blade design.

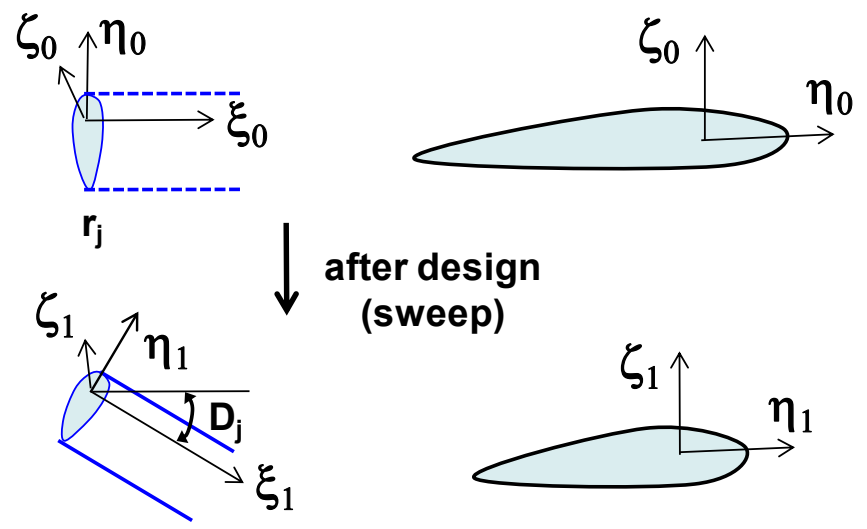


Figure 2. Cross-sectional coordinates before and after parametric design.

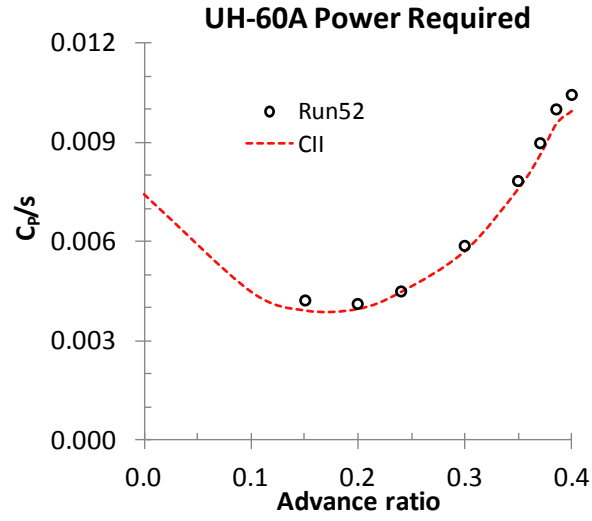


Figure 3. Correlation of the UH-60A main rotor power polar in a full speed range.

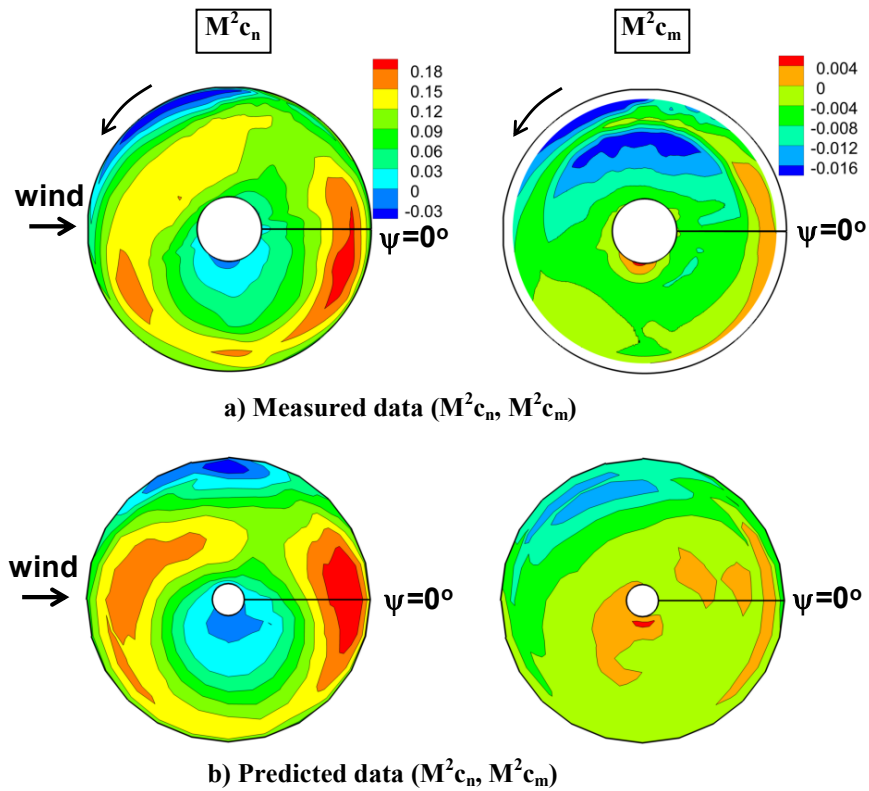


Figure 4. Contours of the measured and predicted UH-60A  $M^2c_n$  and  $M^2c_m$  (Run 52, Point 31,  $\mu=0.30$ ).

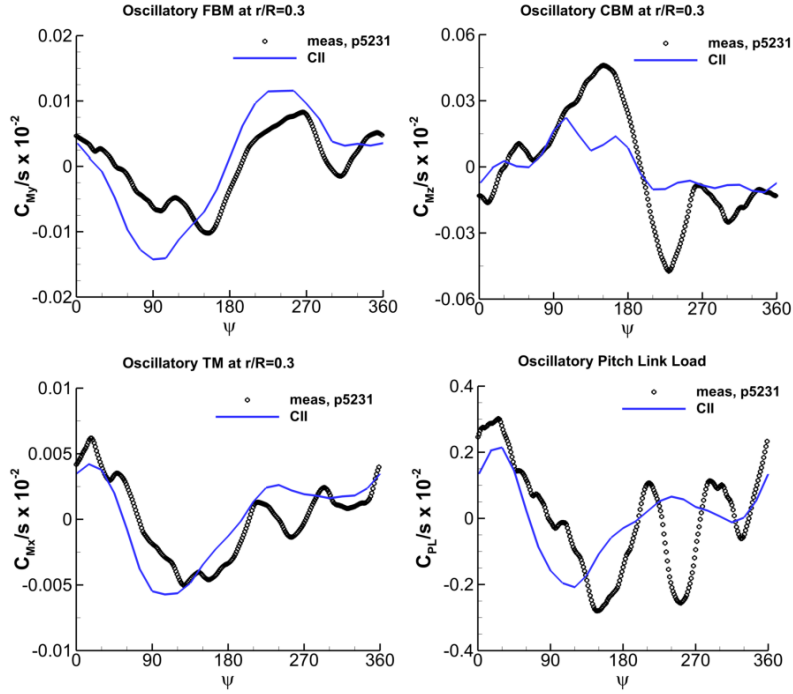


Figure 5. Correlation of the oscillatory flap bending moment (FBM), chord bending (CBM), torsion (TM) moments at  $r/R=0.30$ , and pitch link load of the UH-60A rotor (Run 52, Point 31,  $\mu=0.30$ ).

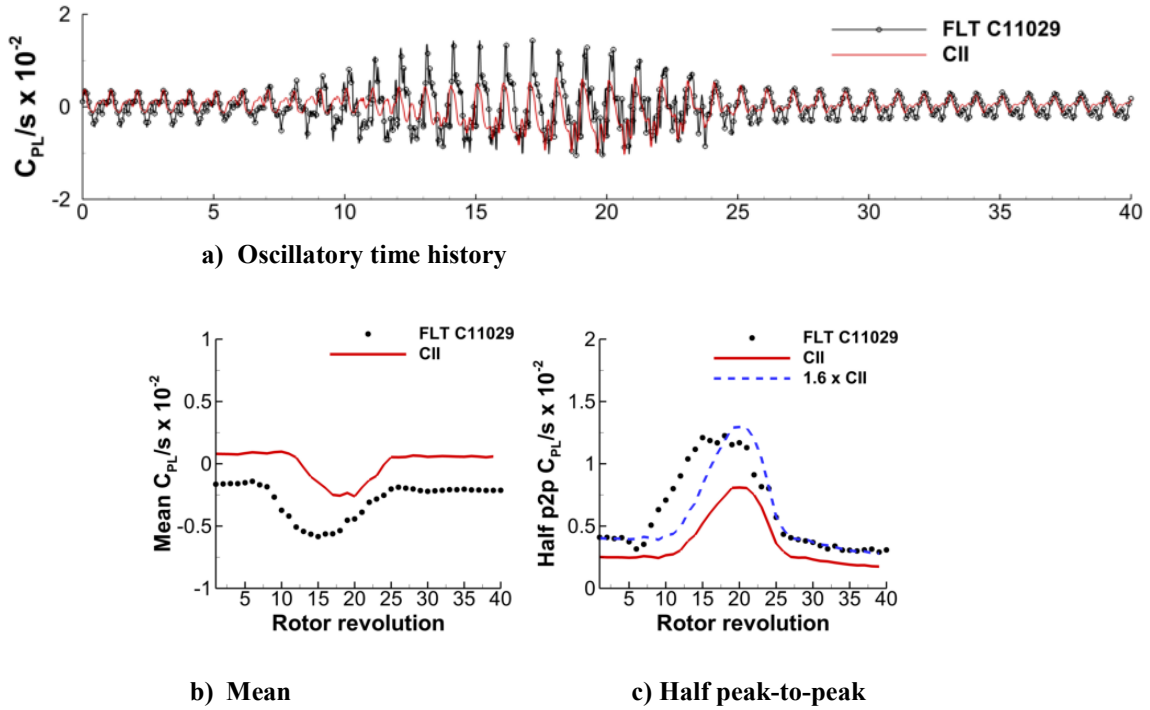


Figure 6. Correlations of a) Oscillatory time history, b) mean, and c) half peak-to-peak of pitch link load during the UTTAS maneuver (C11029).

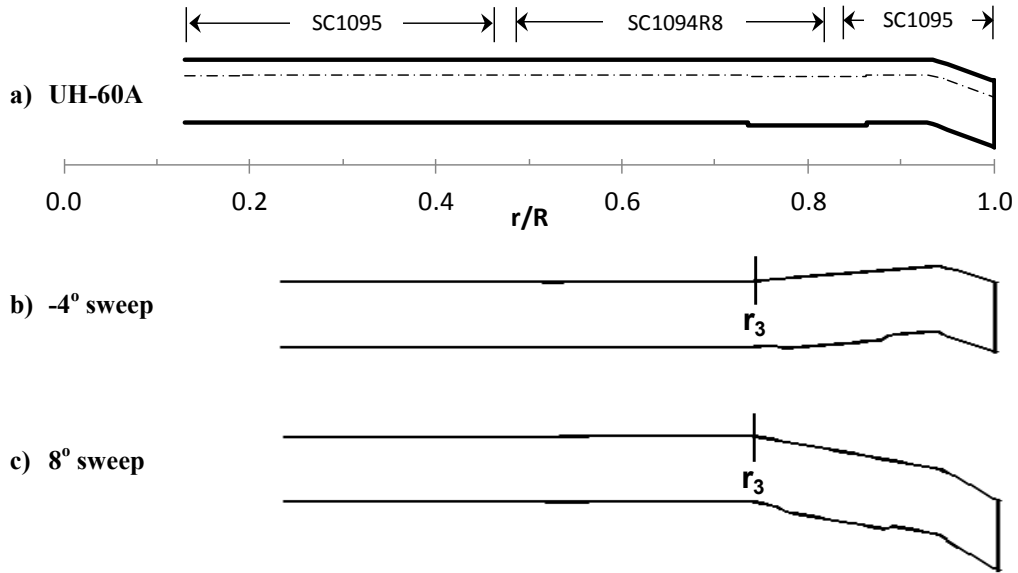


Figure 7. A sketch of the UH-60A blade planform with two parametric blade designs (PD1) – one with  $-4^\circ$  (forward) sweep and the other with  $8^\circ$  (backward) sweep at  $r/R=0.70$  ( $r_3$ ).

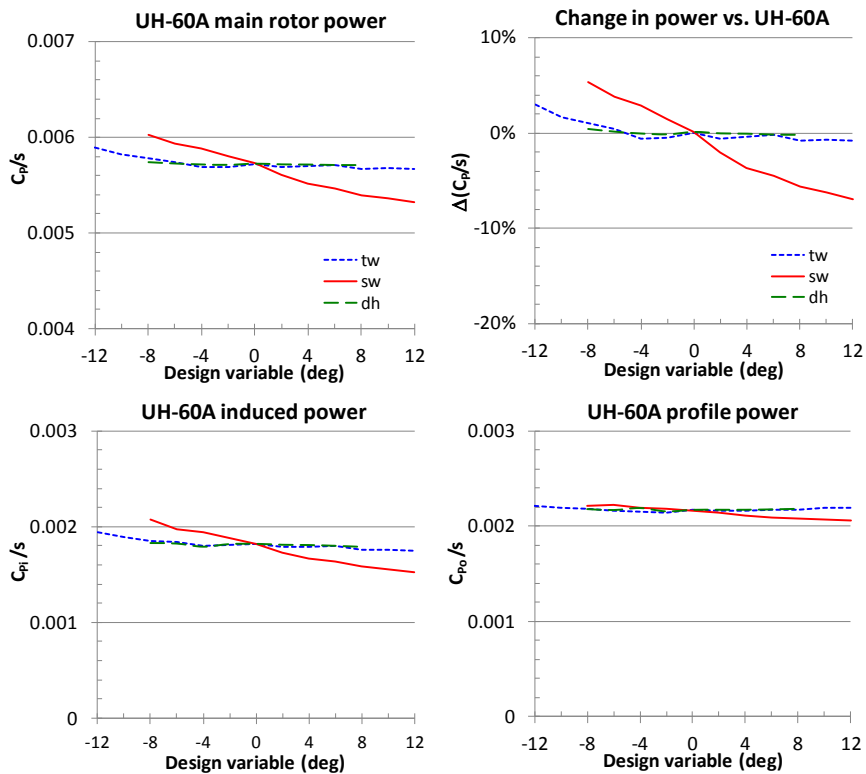


Figure 8. Sensitivity of total power of the UH-60A rotor with twist, sweep, and dihedral at  $r/R=0.70$  (Run 52, Point 31,  $\mu=0.30$ ).

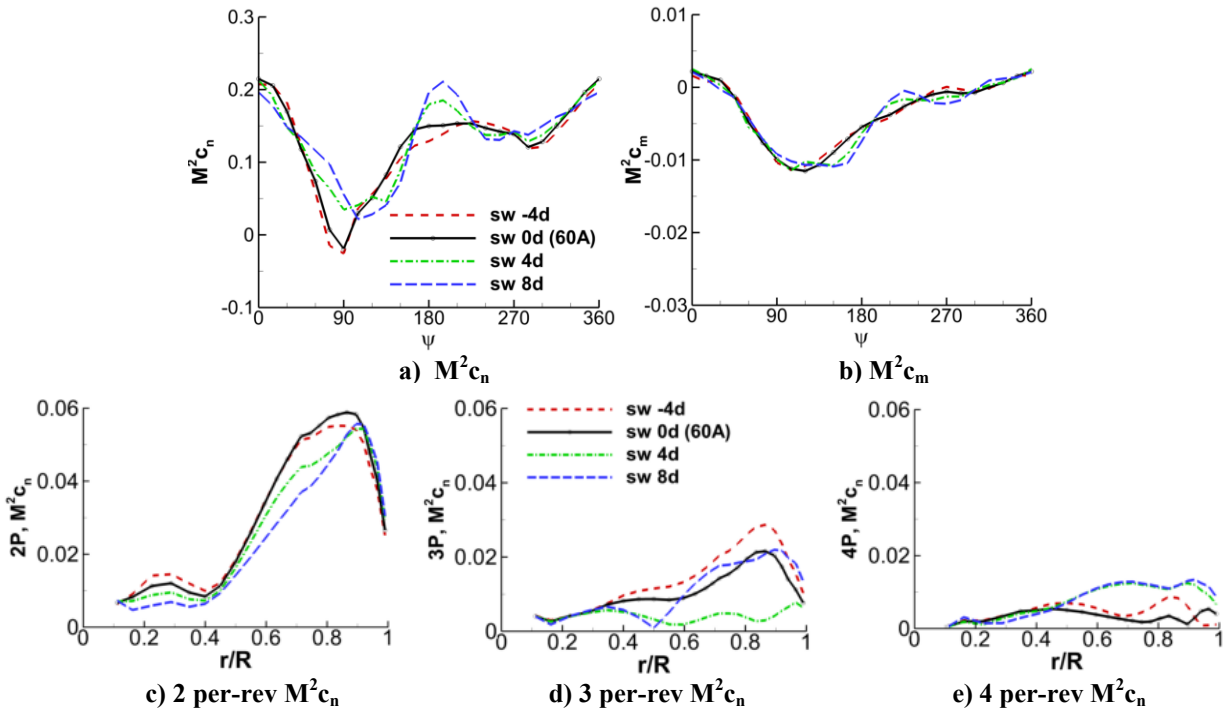


Figure 9. Correlation of  $M^2c_n$  and  $M^2c_m$  of the PD1 rotor with sweep at  $r/R=0.70$  (Run 52, Point 31,  $\mu=0.30$ ).

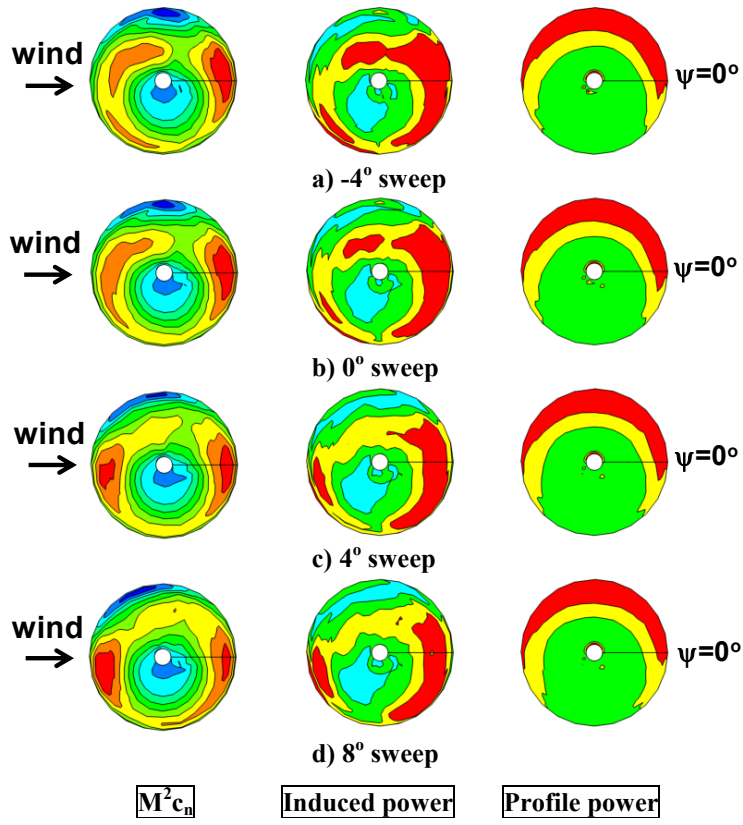


Figure 10. Predicted contours of  $M^2c_n$ , induced power, and profile power of the PD1 rotor with sweep at  $r/R=0.70$  (Run 52, Point 31,  $\mu=0.30$ ). The red color indicates a high value.

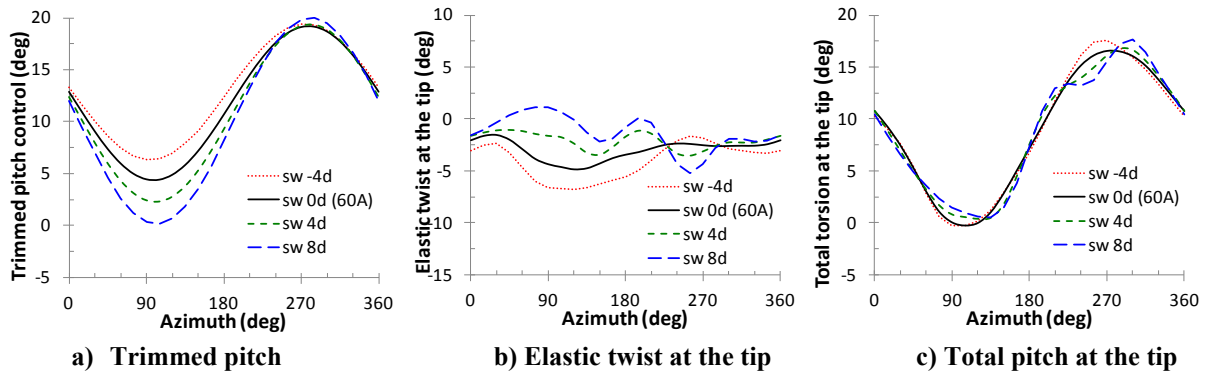


Figure 11. Torsion responses of the PD1 rotor with sweep at  $r/R=0.70$  (Run 52, Point 31,  $\mu=0.30$ ).

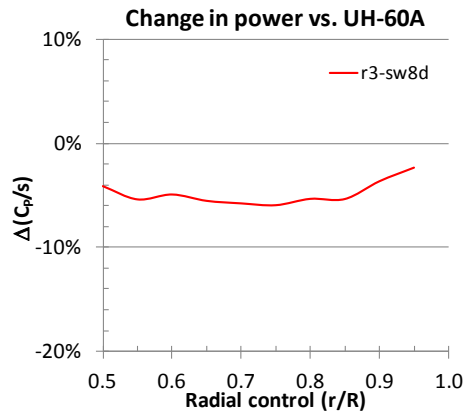


Figure 12. Total power of the PD1 rotor with the radial control point of an  $8^\circ$  sweep varied from  $r/R = 0.50$  to  $0.95$  (Run 52, Point 31,  $\mu=0.30$ ).

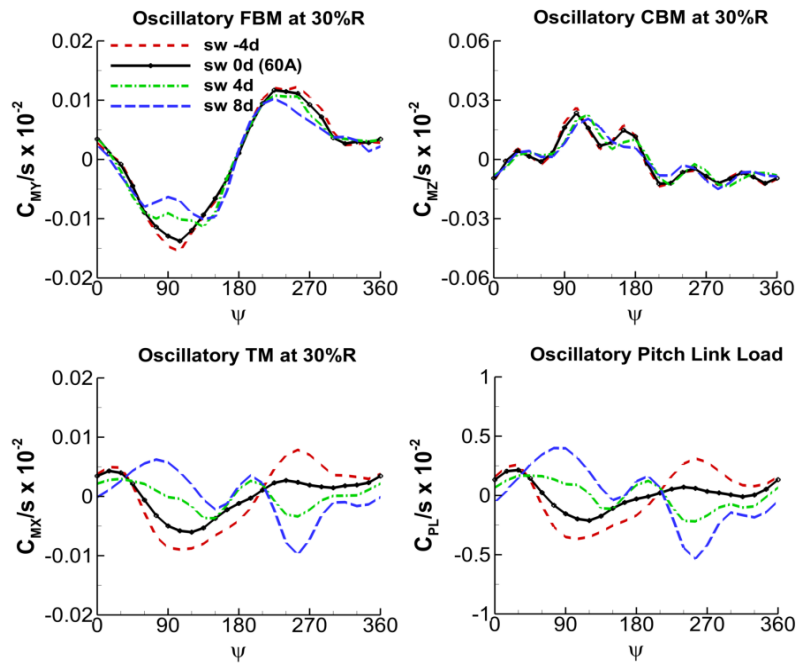


Figure 13. Oscillatory flap bending (FBM), chord bending (CBM), and torsion (TM) moments at  $r/R=0.30$ , and pitch link load (PL) of the PD1 rotor with sweep (Run 52, Point 31,  $\mu=0.30$ ).

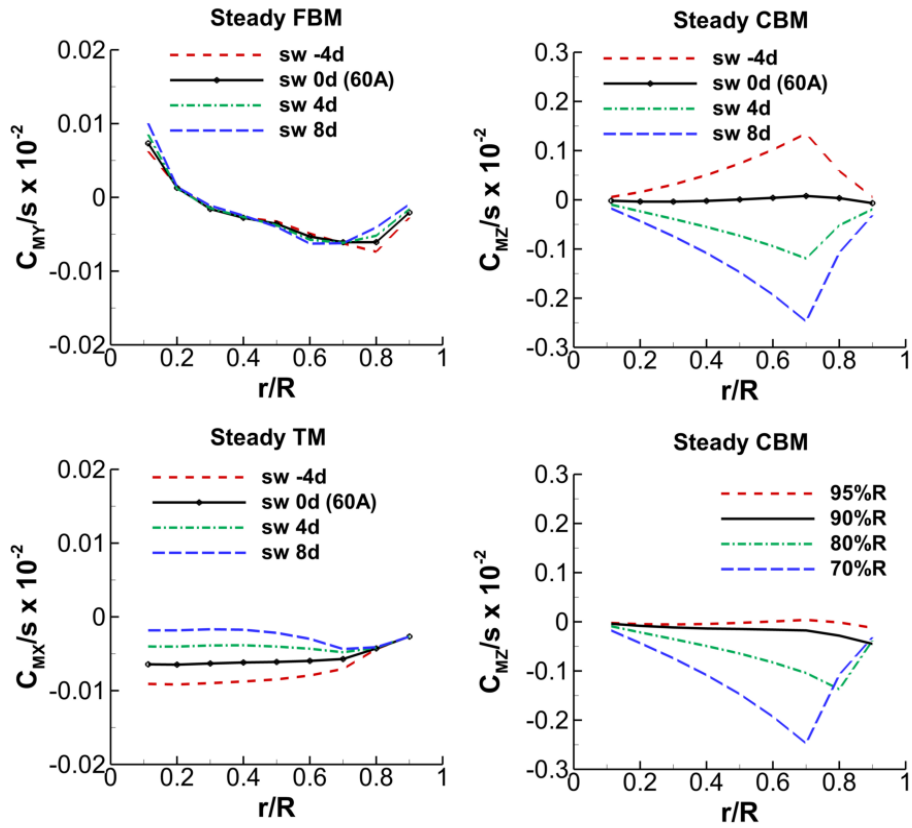


Figure 14. Steady flap bending (FBM), chord bending (CBM), and torsion (TM) moments at  $r/R=0.30$  with sweep variation, and steady CBM with an  $8^\circ$  sweep varied along the blade span for the PD1 rotor (Run 52, Point 31,  $\mu=0.30$ ).

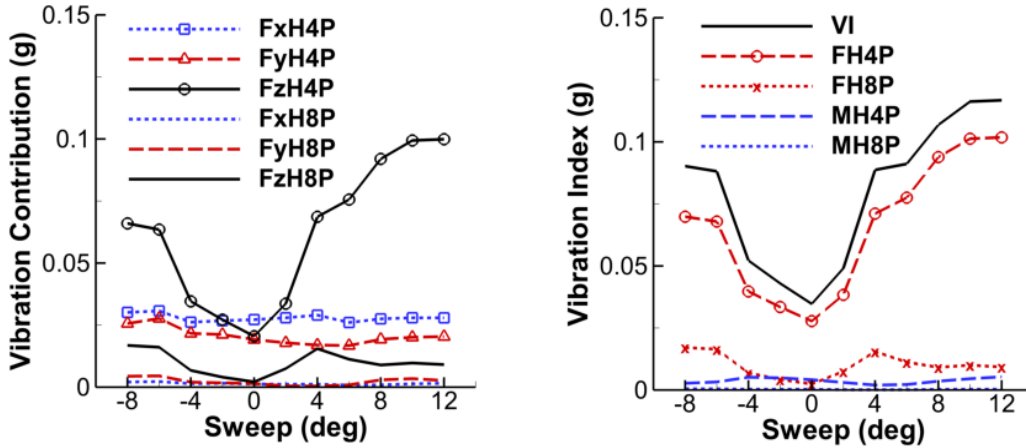


Figure 15. Vibrations contributed from the individual components of the 4 and 8 per-rev hub forces and the vibration index as sweep changes for the PD1 rotor (Run 52, Point 31,  $\mu=0.30$ ).

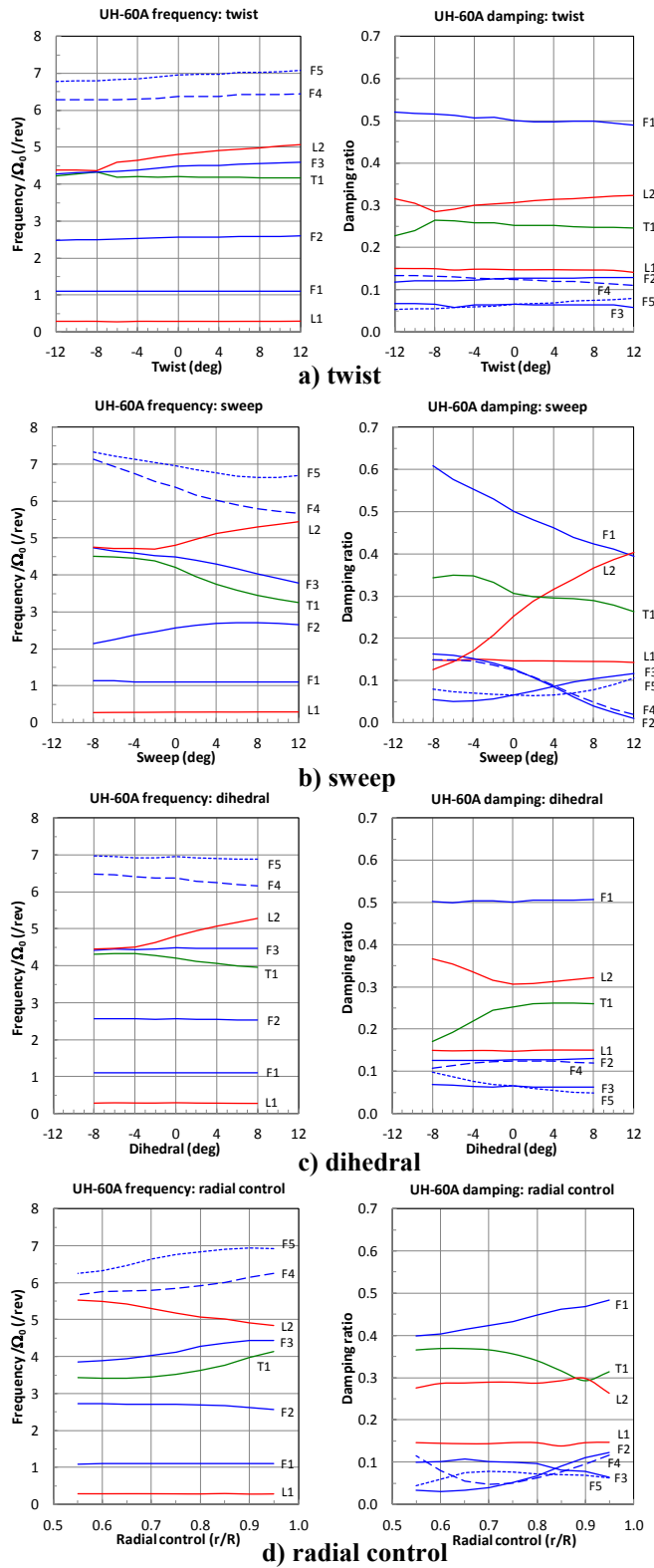


Figure 16. Frequencies and damping ratios of the PD1 rotor with twist, sweep, dihedral, and the radial control point (Run 52, Point 31,  $\mu=0.30$ ).

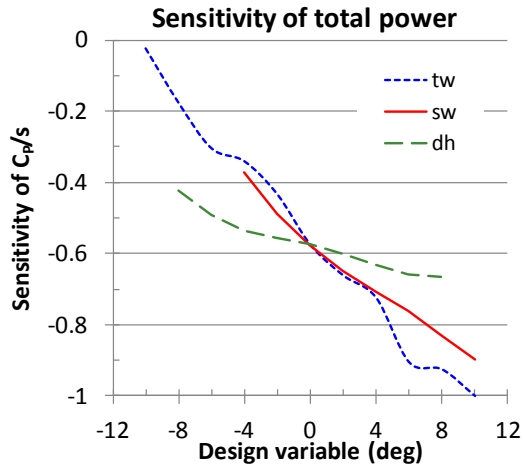


Figure 17. Sensitivity of total power of the UH-60 wide chord blade rotor with twist, sweep, and dihedral at  $r/R=0.70$  (Run 52, Point 31,  $\mu=0.30$ ).

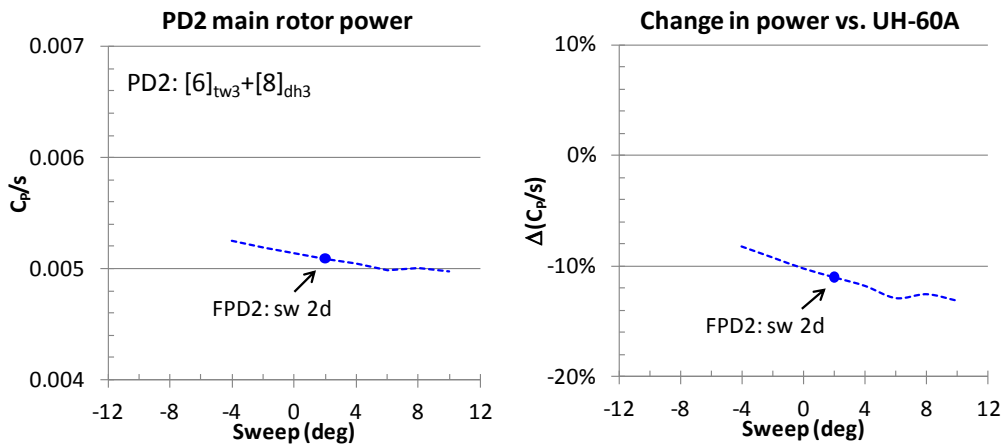


Figure 18. Sensitivity of power of the PD2 design with twist, sweep, and dihedral at  $r/R=0.70$  (Run 52, Point 31,  $\mu=0.30$ ).

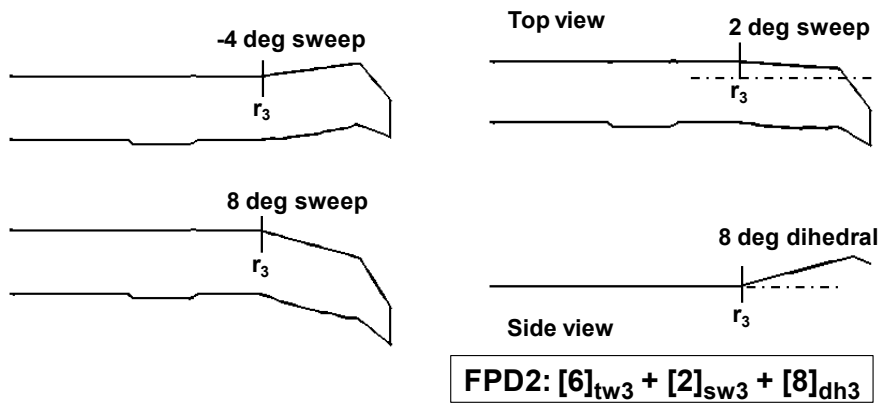


Figure 19. A sketch of the FPD2 rotor blade with sweep variation.

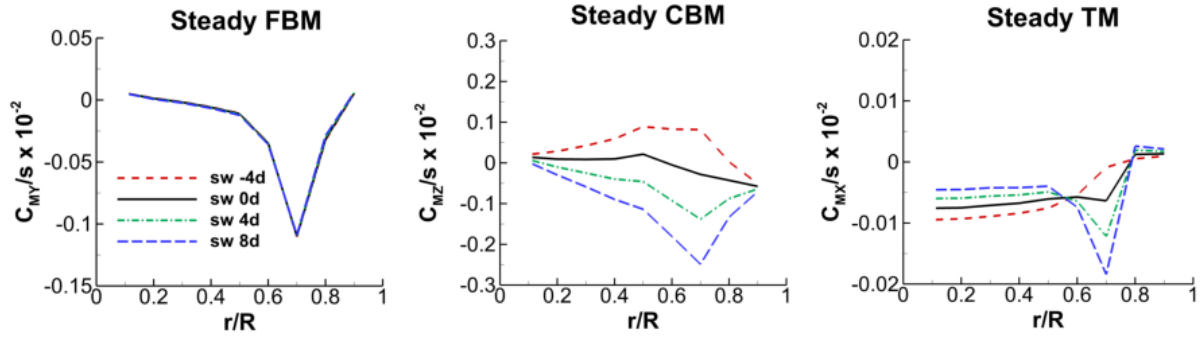


Figure 20. Sensitivity of the steady flap bending (FBM), chord bending (CBM), and torsion (TM) moments at  $r/R=0.30$  of the PD2 rotor with sweep variation at  $r/R=0.70$  (Run 52, Point 31,  $\mu=0.30$ ).

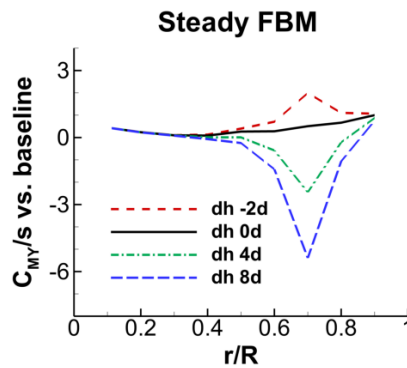


Figure 21. Sensitivity of the steady flap bending moment (FBM) at  $r/R=0.30$  of the PD2 rotor with dihedral variation at  $r/R=0.70$  (Run 52, Point 31,  $\mu=0.30$ ).

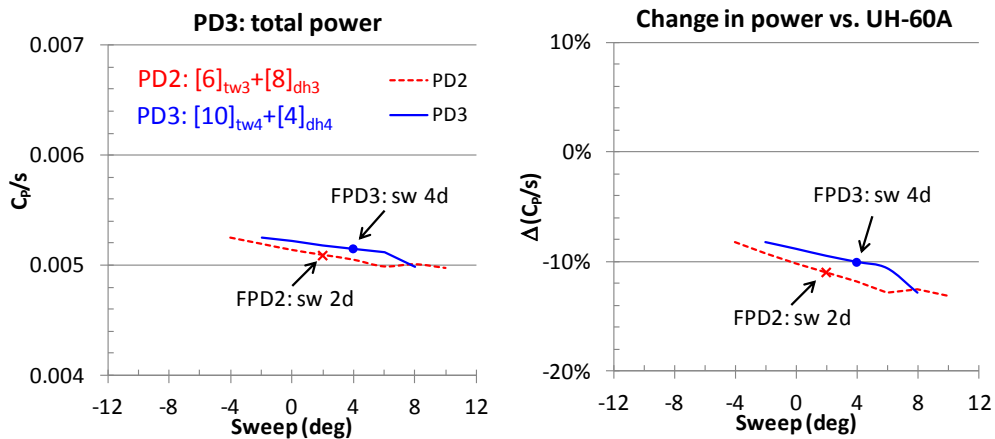


Figure 22. Comparison of total power between the PD2 and PD3 rotors with sweep variation; the sweep was applied at  $r/R=0.70$  for the PD2 rotor and at  $r/R=0.85$  for the PD43 rotor (Run 52, Point 31,  $\mu=0.30$ ).

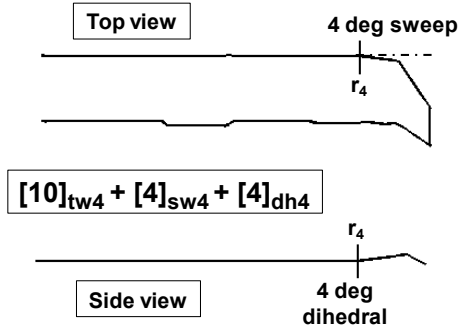


Figure 23. A sketch of the FPD3 rotor blade design.

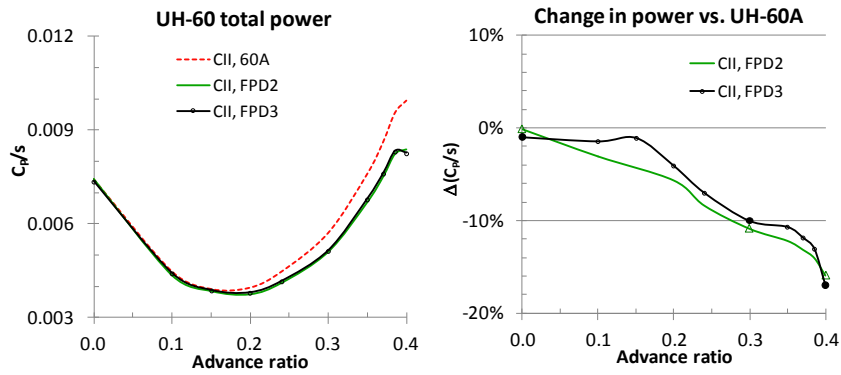


Figure 24. Comparison of power polar between the FPD2 and FPD3 rotors in a full speed range (Run 52).

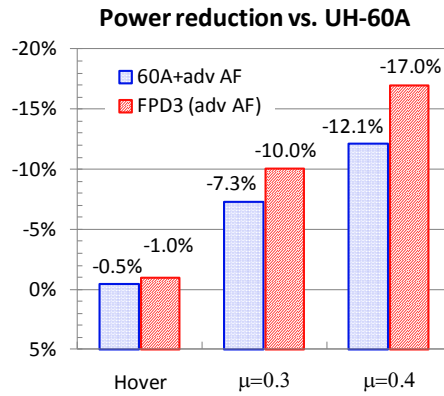


Figure 25. Comparison of total power between the UH-60A with the advanced airfoils and the FPD3 rotor at various speeds.

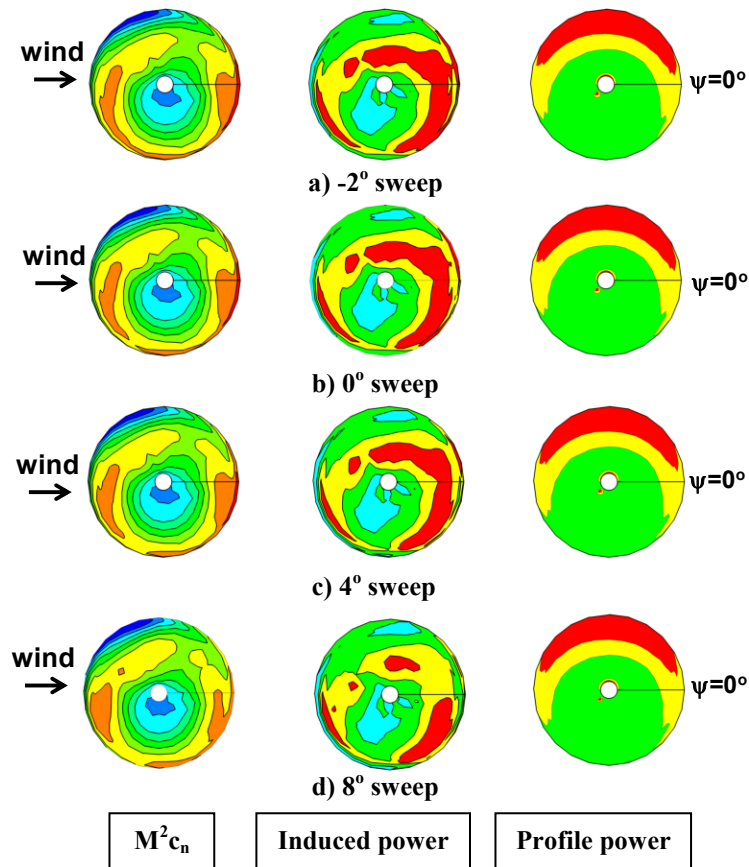


Figure 26. Predicted contours of  $M^2 c_n$  and the induced and profile powers of the PD3 rotor with sweep at  $r/R=0.85$  (Run 52, Point 31,  $\mu=0.30$ ). The red color indicates a high value.

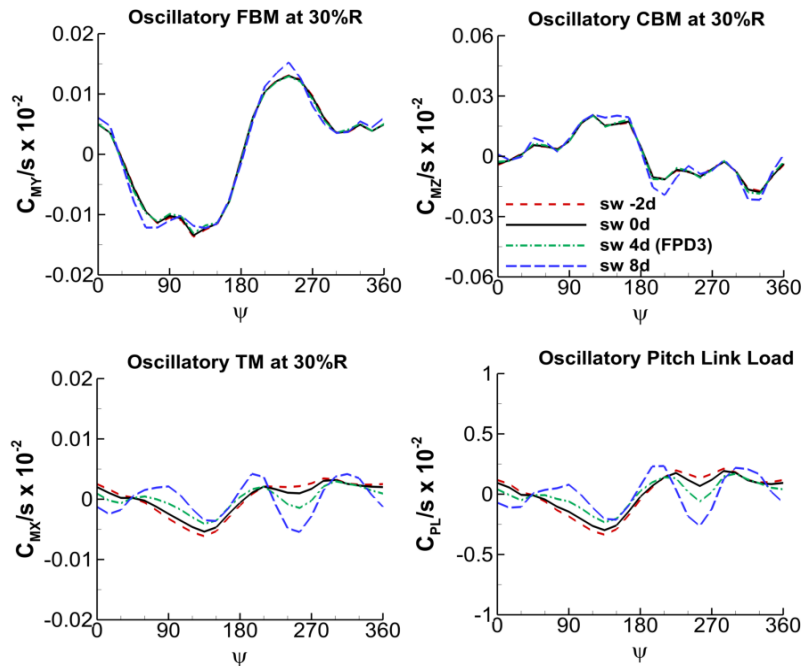


Figure 27. Sensitivity of the oscillatory FBM, CBM, TM at  $r/R=0.30$ , and the oscillatory pitch link load of the PD3 rotor with sweep variation at  $r/R=0.85$  (Run 52, Point 31,  $\mu=0.30$ ).

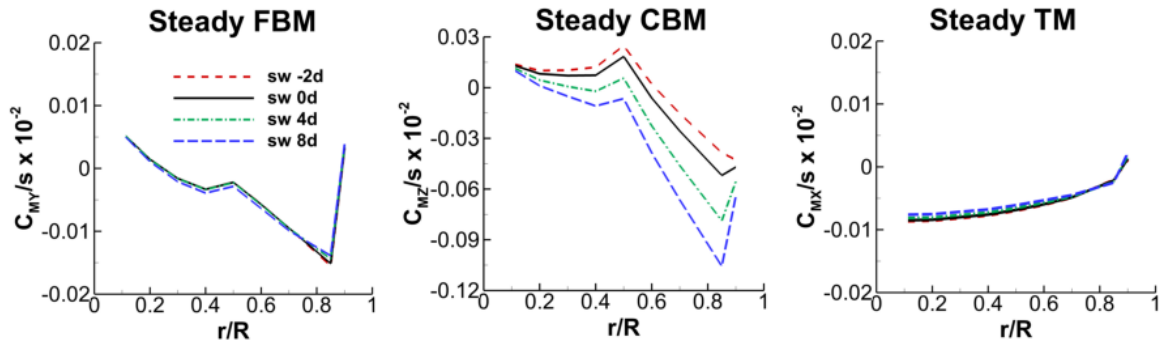


Figure 28. Sensitivity of the steady FBM, CBM, and TM at  $r/R=0.30$  of the PD3 rotor with sweep variation at  $r/R=0.85$  (Run 52, Point 31,  $\mu=0.30$ ).

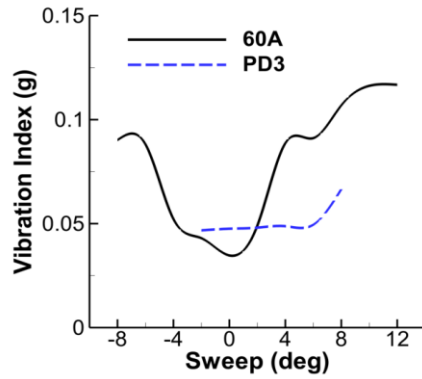


Figure 29. Vibration index between the UH-60A and PD3 rotors with sweep variation (Run 52, Point 31).

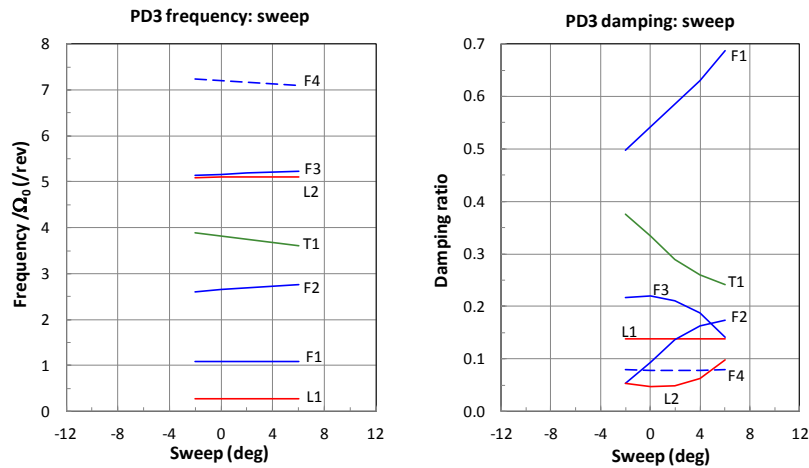
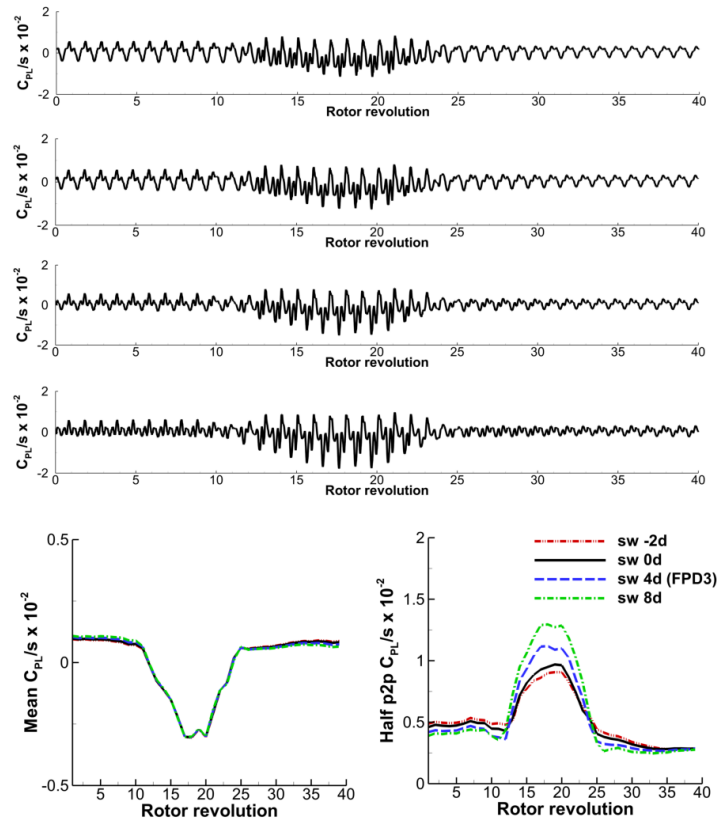


Figure 30. Sensitivity of the frequencies and damping ratios of the PD3 rotor with sweep variation (Run 52, Point 31,  $\mu=0.30$ ).



**Figure 31. Sensitivity of the pitch link load (oscillatory time history, mean, and half peak-to-peak) with sweep variation during the UTTAS maneuver (C11029).**

*COPYRIGHT STATEMENT*

*The author(s) confirm that they, and/or their company or organisation, hold copyright on all of the original material included in this paper. The authors also confirm that they have obtained permission, from the copyright holder of any third party material included in this paper, to publish it as part of their paper. The author(s) confirm that they give permission, or have obtained permission from the copyright holder of this paper, for the publication and distribution of this paper as part of the ERF2014 proceedings or as individual offprints from the proceedings and for inclusion in a freely accessible web-based repository.*